The Astrophysical Journal, 922:108 (9pp), 2021 December 1 https://doi.org/10.3847/1538-4357/ac26c7

Understanding the Initiation of the M2.4 Flare on 2017 July 14

Ju Jing, Satoshi Inoue, Jeongwoo Lee, Qin Li, Gelu M. Nita, Yan Xu, Chang Liu, Dale E. Gary, and Haimin Wang
Institute for Space Weather Sciences, New Jersey Institute of Technology, University Heights, Newark, NJ 07102-1982, USA; ju.jing@njit.edu
Received 2021 April 8; revised 2021 September 13; accepted 2021 September 13; published 2021 November 24

Abstract

We present both the observation and the magnetohydrodynamics (MHD) simulation of the M2.4 flare (SOL2017-07-14T02:09) of NOAA active region (AR) 12665 with a goal to identify its initiation mechanism. The observation by the Atmospheric Image Assembly (AIA) on board the Solar Dynamics Observatory (SDO) shows that the major topology of the AR is a sigmoidal configuration associated with a filament/flux rope. A persistent emerging magnetic flux and the rotation of the sunspot in the core region were observed with Magnetic Imager (HMI) on board the SDO on the timescale of hours before and during the flare, which may provide free magnetic energy needed for the flare/coronal mass ejection (CME). A high-lying coronal loop is seen moving outward in AIA EUV passbands, which is immediately followed by the impulsive phase of the flare. We perform an MHD simulation using the potential magnetic field extrapolated from the measured pre-flare photospheric magnetic field as initial conditions and adopting the observed sunspot rotation and flux emergence as the driving boundary conditions. In our simulation, a sigmoidal magnetic structure and an overlying magnetic flux rope (MFR) form as a response to the imposed sunspot rotation, and the MFR rises to erupt like a CME. These simulation results in good agreement with the observation suggest that the formation of the MFR due to the sunspot rotation and the resulting torus and kink instabilities were essential to the initiation of this flare and the associated coronal mass ejection.

Unified Astronomy Thesaurus concepts: Solar activity (1475); Solar flares (1496); Solar active region magnetic fields (1975)

Supporting material: animations

1. Introduction

Magnetically driven solar flares and coronal mass ejections (CMEs) are the most energetic solar eruptions, and play a key role in space and terrestrial environments. In flare-prone solar active regions (ARs), free magnetic energy is accumulated and stored in the coronal magnetic field, and then can be abruptly released to power flares/CMEs (Priest & Forbes 2002; Shibata & Magara 2011). An important yet unresolved issue in this energy storage-and-release scenario is the initiation mechanism of energy release. Based on the framework of the standard flare model (known as the CHSKP model; Carmichael 1964; Sturrock 1966; Hirayama 1974; Kopp & Pneuman 1976), numerical magnetohydrodynamic (MHD) models for solar eruptions have been developed, which can shed light on the potential initiation mechanisms of flares/CMEs. Theoretically, the initiation could be via an ideal MHD process whereby torus and/or kink instabilities (Török & Kliem 2005; Kliem & Török 2006; Kliem et al. 2013) drive the eruptions without the need for a reconfiguration in magnetic topology, or it could be a resistive MHD process invoking magnetic reconnection in topologically complex fields to trigger eruptions, as in the magnetic breakout model (Antiochos et al. 1999; Karpen et al. 2012). The positive feedback between the MHD instabilities and magnetic reconnection can also occur (Zhang & Dere 2006; Welsch 2018), which is referred to as "reconnective instability" (Welsch 2018), and such instability may be effective in accelerating CMEs.

These eruption scenarios are supported not only by simulations but also by interpretations of observations and laboratory experiments. The ideal MHD torus and kink instabilities are often characterized by two parameters in solar magnetic field, decay index and magnetic twist, respectively, which are found to be viable in explaining solar eruptions, especially in assessing the likelihood of a successful eruption (Myers et al. 2015; Sun et al. 2015; Jing et al. 2018). A recent model by Amari et al. (2018) attributes the key triggering mechanism to the formation of a twisted magnetic flux rope (MFR) that becomes unstable and breaks through the overlying field. On the other hand, magnetic reconnection is related to the topological complexity of magnetic structures and may manifest itself in some flare observations (e.g., Demoulin et al. 1993; Liu et al. 2012, 2013; Li et al. 2016). There is mounting observational evidence for the important role of small-scale reconnections near the magnetic polarity inversion line (PIL) in triggering solar eruptions (Chen et al. 2014; Wang et al. 2017). Such a localized, near-surface reconnection is associated with small-scale magnetic configurations categorized as opposite magnetic polarity (OP) or reversed shear (RS) structures (Kusano et al. 2012), and may represent a tether-cutting-like reconnection (Moore et al. 2001). In a recent kinematic model by Ishiguro & Kusano (2017), a double-arc-shaped loop formed by tether-cutting reconnection is found to be more easily destabilized than an axisymmetric single-arc loop, known as double-arc instability. Another recent simulation by Wyper et al. (2017) accommodates both ideal MHD instabilities and those caused by resistive magnetic reconnection, and suggests that magnetic breakout is the universal model applicable for solar eruptions from small-scale jets to stellar-scale CMEs.

Observationally it is of interest how a solar AR evolves to reach the condition for the eruption. It has been known that sunspot rotation (Evershed 1909) could be one of the causes. The connection between rotating sunspots and eruptive activity has been widely reported (e.g., Hiremath 2006;

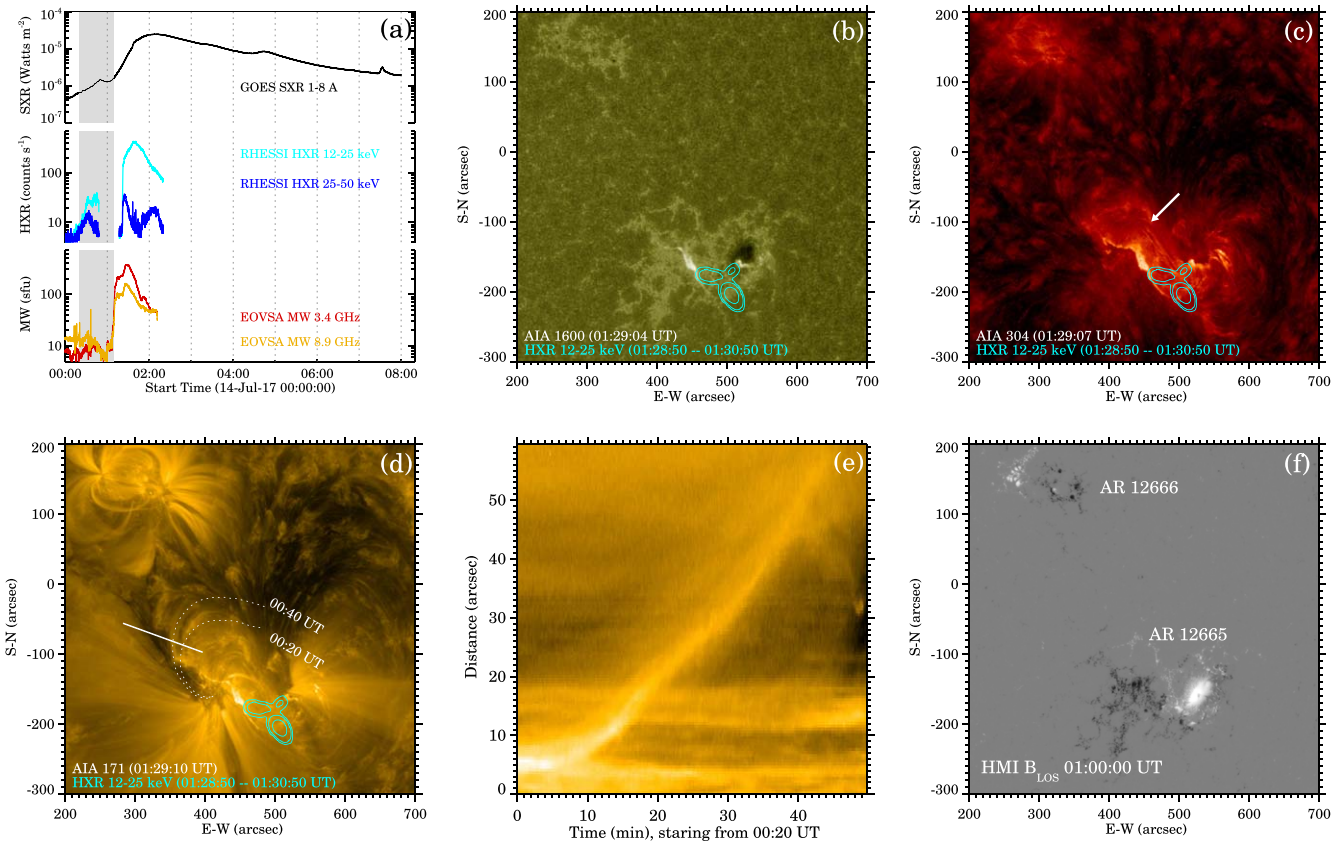

Figure 1. Overview of the M2.4 flare and the hosting AR 12665. (a) Light curves of GOES SXR 1–8 Å (black), RHESSI HXR 12–25 KeV (blue), and EOVSA MW 3.4 GHz (red). The gray shaded area indicates the time window of the outward motion of the coronal loop. (b)–(d) Snapshots of AIA 1600 Å 304 Å and 211 Å all taken at the impulsive phase of the flare, on 2017 July 14, at 01:29 UT. The green contours show RHESSI HXR intensity integrated in the time intervals 01:28:50-01:30:50 UT, in the 6–12 keV energy range. The contour levels are 20%, 25%, and 50% of the intensity maximum. The arrow in (c) points to a filament. The two dotted curves in (d) outline the visible locations of the outward moving coronal loop at two different times. The solid line in (d) denotes the slit used to derive the time–distance stackplot displayed in (e). (f) Pre-flare HMI line-of-sight (LOS) magnetogram, overlaid with the flaring magnetic polarity inversion line (PIL). A 34 s animation is available that shows the image sequences of AIA 304 Å and 171 Å from July 14, 00:00 UT to 03:30 UT. The GOES SXR flux lightcurve is shown in the top panel of the animation, with a moving vertical line indicating the time.

(An animation of this figure is available.)

Suryanarayana 2010; Yan et al. 2012; Liu et al. 2016). An MHD simulation of a sunspot rotation leading to a CME shows that sunspot rotation can substantially weaken the stabilizing magnetic tension above an MFR, especially in ARs where the sunspot is dominant (Török et al. 2013).

In this paper, we focus on a specific flare event, the M2.4 flare of NOAA AR 12665, to understand its initiation mechanism. This flare is associated with a fast halo CME and produces a solar energetic particle (SEP) storm at 1 au. We present both observations and an MHD simulation of the flare in Sections 2 and 3, respectively, and conclude in Section 4.

2. Observation

The flare that we discuss in this paper appeared in NOAA AR 12665 on 2017 July 14 (44°W, 7°S). We use EUV/UV images obtained from the Atmospheric Image Assembly (AIA; Lemen et al. 2012) on board the Solar Dynamics Observatory (SDO) to study the flare morphology and coronal topology, and use magnetogram data obtained from the SDO/Heliospheric and Magnetic Imager (HMI; Schou et al. 2012) to study the evolution of magnetic field. Figure 1 gives an overview of the flare and the hosting AR. This AR shows well-separated polarities, with a leading sunspot of positive magnetic flux that dominates the region and a trailing magnetic plage of negative flux (Figure 1(f)). The AR exhibits nonpotential signatures most clearly in the sigmoid configuration in the AIA EUV observations (Figure 1(d) and the corresponding animation), which is probably associated with the dark filament seen in the AIA 304 Å image (Figure 1(c)). The flare emission starts at 01:07 UT, reaches its maxima at 02:09 UT, and ends at 03:24 UT in GOES soft X-ray (SXR) 1–8 Å flux, and shows a peak in RHESSI hard X-ray (HXR) 25–50 KeV and EOVSA microwave (MW) 8.9 GHZ at about 01:29 UT (Figure 1(a)). The flare exhibits two ribbons, though the western ribbon is short and moves across the sunspot umbra (Figure 1(b)). The RHESSI HXR 12–25 keV contour at the impulsive phase of the flare shows a roughly cusp-shaped arcade covering the loop top and the two footpoints (Figures 1(b)–(d)).

Inspection of the AIA EUV image sequences reveals that a high-lying coronal loop over the sigmoidal structure expands outward immediately prior to the impulsive phase of the flare (see the animation of Figure 1). This outward motion of the coronal loop is visible at the AIA passbands most sensitive to the temperatures of the quiet-Sun corona such as 171, 193, and 211 Å (Figure 1(d)). One end of the loop emanates from the negative polarity field, at the periphery of the eastern ribbon of the flare. The other end, though not clearly visible, presumably connects to the sunspot of positive polarity. To detect the

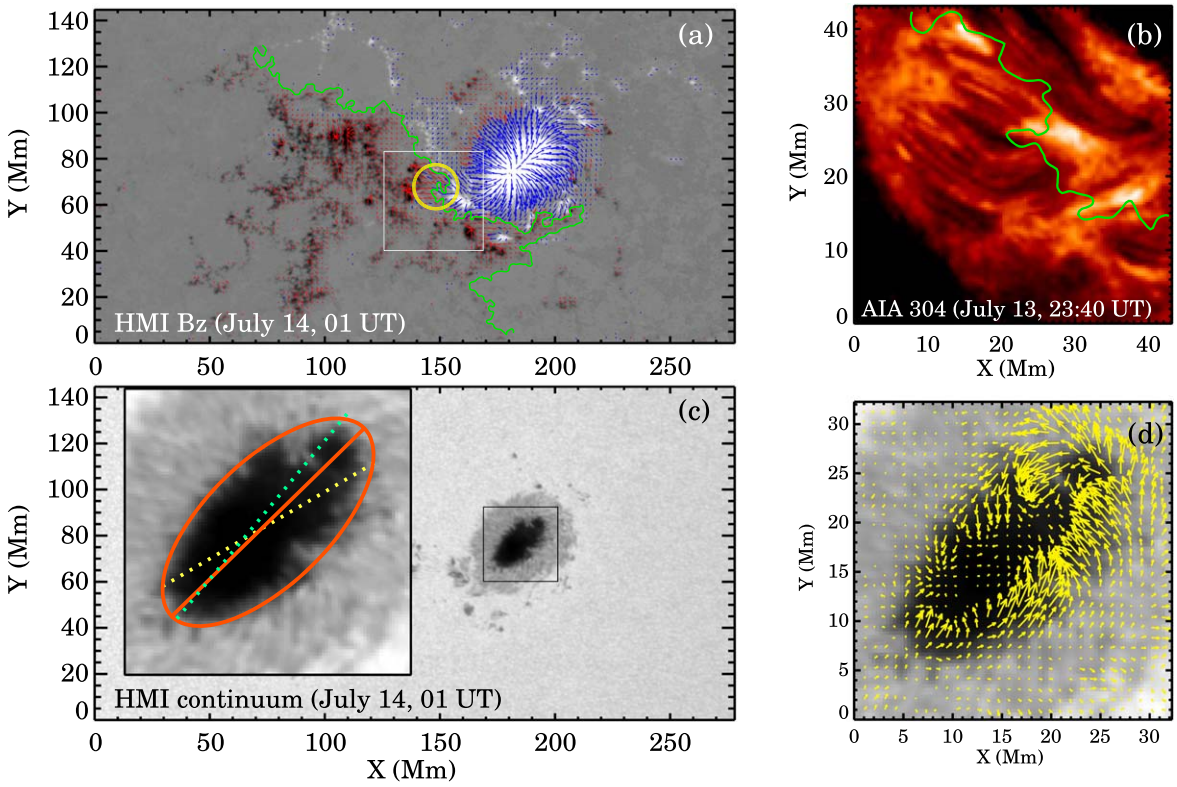

Figure 2. Magnetic field of AR 12665. (a) HMI vertical magnetic field B_z at 01 UT, 2017 July 14, superimposed with arrows displaying the horizontal magnetic field and the green contour representing the major flaring PIL. The box denotes the region of flux emergence and defines the field of view of (b). The yellow circle indicates a typical OP structure. (b) AIA 304 Å snapshot at 23:40 UT, July 13, remapped with the CEA projection, and superimposed with the PIL of 23:36 UT, July 13. (c) HMI continuum image at 01 UT, July 14. The box enclosing the sunspot region is zoomed in and displayed in the inset and in (d). The red ellipse represents an ellipse fit to the umbra of 01 UT, July 14, and the red line represents its major axis. The yellow and green dotted lines represent the major axis of the ellipses fitted to the umbra at 16 UT, July 13, and 04 UT, July 14, respectively. (d) The continuum image, superimposed with arrows illustrating counterclockwise rotational flows averaged between July 13, 16 UT and July 14, 04 UT. A 2 s animation is available that shows the image sequences of HMI B_z (left) and continuum (right), from July 13, 16:00 UT to July 14, 08:00 UT.

(An animation of this figure is available.)

motion of the coronal loop, Figure 1(e) shows the time–distance map constructed from the slit denoted in Figure 1(d). The typical speed of the projection is approximately 20 km s^{-1}, as it moves a distance of ∼30 Mm in 25 minutes. This speed is much slower than the speed of the associated CME (1200 km s^{-1}). However, it should be noted that the CME speed measures the propagation of the rapidly expanding frontal loop of the CME, whereas the speed derived from the time–distance map here measures the motion of a coronal loop seen on the disk, and they may represent different aspects of the eruption. Moreover, given the position of the measurement close to the disk center, this speed may be greatly underestimated due to the projection effects. On the other hand, despite the mass motion visible in the coronal loop, the filament underneath does not erupt, but disappears gradually during the flare most likely due to the increase in the filament's temperature, and reappears several hours after the flare.

The animation of Figure 2 shows the field evolution of the AR over a period of 15 hr, from 2017 July 13, 16 UT, to July 14, 07 UT, with the HMI data (`hmi.sharp_cea_720s`; Bobra et al. 2014). Magnetic flux emergence takes place at the major magnetic PIL ∼3 hr prior to the flare, and continues until the end of the animation. The newly emerged flux is of the OP structure (Figures 2(a)–(b)) as described in Kusano et al. (2012), which is seemingly a favorable configuration for a magnetic reconnection-induced eruption process (Kusano et al. 2012). Sporadic localized brightenings occur in the area of flux emergence before the flare, but none of them is immediately associated with the onset of the flare (Figure 2(b)). The field evolution also features the counterclockwise rotation of the leading sunspot during the entire period of the animation. We measured the rotation with the cylindrical equal area (CEA; Thompson 2006) projected continuum maps from HMI. For the sake of simplicity, the rotation of the sunspot is roughly evaluated by an ellipse fitting to the umbra region at different times under a rigid rotation assumption (Liu et al. 2016). The rotation of the major axis covers a total angular range of ∼25° for a period of 12 hr (Figure 2(c)), resulting in an average rotation rate of ∼2°h^{-1} in the umbra. This is consistent with the average rotational rate reported in the past (Brown et al. 2003). We also track the continuum flows with the local correlation tracking (LCT) method. The flow map clearly shows a counterclockwise rotational pattern around the edge of the umbra, especially at the top portion (Figure 2(d)).

Magnetic flux emergence and sunspot rotation may have contributed to the energy buildup of the AR. To calculate the free magnetic energy ($E_{\rm free} = \int B^2_{\rm NLFFF} dV - \int B^2_{\rm potential} dV$) stored in the AR, we extrapolate the three-dimensional (3D) NLFFF and potential field from the photospheric magnetic field boundary conditions. The HMI data were rebinned to 1.45 Mm pixel scale and transformed to a local Cartesian coordinate system using the same CEA projection that is used to produce

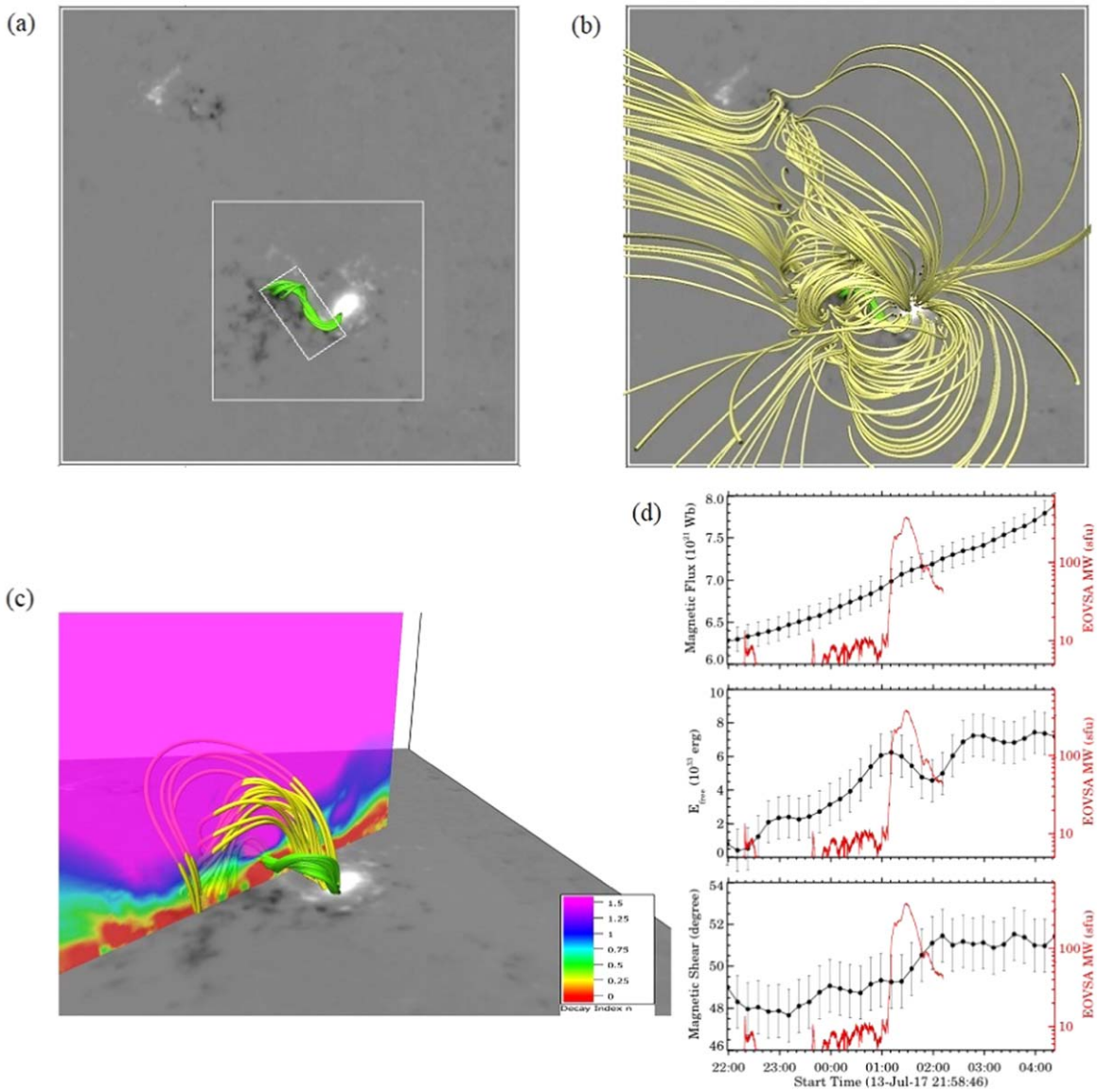

Figure 3. NLFFF of AR 12665. (a)–(b) HMI vertical magnetic field B_z at 01 UT, 2017 July 14, with NLFFF lines overlaid. The MFR over the flaring PIL is plotted in green, and other field lines are plotted in yellow. The large square box in (a) defines the region (∼220 Mm × 220 Mm × 145 Mm) for the calculation of free magnetic energy, and the rectangle box defines the region (∼44 Mm × 88 Mm) for the calculation of magnetic flux and shear angle. (c) Side view of the MFR and some arcade field lines. The vertical cross section shows the decay index distribution. (d) Temporal variation of total unsigned magnetic flux, free magnetic energy, shear angle, and EOVSA MW 3.4 GHz lightcurve (red).

the standard `hmi.sharp_cea_720s` data series. Then we use the weighted optimization code ("AS code"; see Fleishman et al. 2017 for definitions and details) in the `GX_Simulator` package for NLFFF extrapolation and a fast Fourier transform (FFT) method for potential field extrapolation. The performance of this optimization code for the NLFFF extrapolation was tested by performing a "voxel-by-voxel" comparison between the reconstructed magnetic field and a full-fledged MHD model (Fleishman et al. 2019). The extrapolation is performed within a box of $348 \times 348 \times 348$ uniform grid points, corresponding to $\sim 505 \times 505 \times 505$ Mm. The domain-averaged $|\nabla \cdot \boldsymbol{B}|$ and the current-weighted average of $\sin\theta$ (Wheatland et al. 2000), where θ is the angle between the current density $\boldsymbol{J}$ and $\boldsymbol{B}$, are 3×10^{-9} G cm^{-1} and 0.43, respectively. The former is practically zero, and the latter corresponds to an angle of $\sim 25°$.

The pre-flare NLFFF shows the presence of a bundle of twisted field lines over the PIL (Figure 3(a)), which has a twist number ($T_w = \frac{1}{4\pi}\int_L \alpha dl$) of -3, suggestive of a twisted MFR configuration. The location and the shape of this MFR matches the filament seen in the AIA 304 Å images. The torus instability (Kliem & Török 2006) may occur when the strapping field above the MFR decays rapidly enough with height, typically with a critical decay index ($n = -\frac{\partial \log(B_h)}{\partial \log(h)}$) of 1.5 (Kliem & Török 2006; Aulanier et al. 2010) beyond which the configuration is unstable. A wider range of $0.5 < n_{\rm crit} < 2$ (Fan & Gibson 2007; Démoulin & Aulanier 2010; Fan 2010; Olmedo & Zhang 2010; Zuccarello et al. 2015; Jing et al. 2018) is also suggested in a number of analytical/numerical studies. Following the proposition of the torus instability, we calculate the decay index and find that the MFR definitely remains in the torus-stable regime, with $n < 0.25$ (Figure 3(c)), while the overlying yellow loops are in the torus-unstable regime

($n \geqslant 1.5$). This is in accordance with the observation that the filament, even when perturbed, does not erupt during the flare, whereas an overlying coronal loop erupts. We also calculate the magnetic shear angle around the magnetic PIL, which is defined as the azimuth difference between the observed magnetic field and its potential field. Figure 3(d) shows the temporal evolution of unsigned magnetic flux, free magnetic energy ($E_{\rm free}$), and magnetic shear from 3 hr before to 1 hr after the flare. The magnetic shear angle increases slightly during this period. The time profile of the magnetic flux shows a monotonically increasing trend over the whole period, while that of free magnetic energy shows the buildup of energy before the flare, and then the release of part of free energy synchronous with the impulsive phase of the flare, and then accumulation after the impulsive phase ends.

The key features in the observation that we consider important for the interpretation of the initiation of the eruption are recapitulated as follows: continuous magnetic flux emergence and sunspot rotation before the flare provide sufficient free magnetic energy accounting for the flare/CME; the major topology of the AR is of a sigmoidal configuration; a high-lying coronal loop above the sigmoid is seen moving outward prior to the flare.

3. MHD Simulation

To gain insight into the initiation mechanism of this flare, we perform the zero-beta 3D MHD simulation of solar eruptions that is extensively described in Inoue et al. (2014) and Inoue et al. (2016). We use the following equation set:

$$\frac{\partial \rho}{\partial t} = -\nabla \cdot (\rho \boldsymbol{v}) + \xi \nabla^2 \rho, \tag{1}$$

$$\frac{\partial \boldsymbol{v}}{\partial t} = -(\boldsymbol{v} \cdot \nabla)\boldsymbol{v} + \frac{1}{\rho}\boldsymbol{J} \times \boldsymbol{B} + \nu \nabla^2 \boldsymbol{v}, \tag{2}$$

$$\frac{\partial \boldsymbol{B}}{\partial t} = \nabla \times (\boldsymbol{v} \times \boldsymbol{B} - \eta \boldsymbol{J}) - \nabla \phi, \tag{3}$$

$$\boldsymbol{J} = \nabla \times \boldsymbol{B}, \tag{4}$$

$$\frac{\partial \phi}{\partial t} + c_{\rm h}^2 \nabla \cdot \boldsymbol{B} = -\frac{c_{\rm h}^2}{c_{\rm p}^2}\phi, \tag{5}$$

where ρ is plasma density, $\boldsymbol{v}$ is plasma velocity, $\boldsymbol{B}$ is coronal magnetic field, $\boldsymbol{J}$ is current density, and ϕ is a convenient potential to remove the error deviated from $\nabla \cdot \boldsymbol{B} = 0$. ν and η are viscosity and electric resistivity, which are set to 1.0×10^{-3} and 1.0×10^{-5}, respectively. ξ is a diffusion coefficient for density introduced to reduce any extreme density variations for the stability of the calculation. The length, magnetic field, plasma density, velocity, and time are normalized by L_0, B_0, ρ_0, $V_A = B_0/\sqrt{\mu_0 \rho_0}$, and $\tau = L_0/V_A$, respectively.

We first extrapolate the potential field from the pre-flare photospheric boundary (at 01 UT on 2017 July 14) same as that used for the NLFFF extrapolation (Figure 3(a)). In this MHD simulation, we use the potential field rather than the NLFFF as the initial condition. The reason for this choice is that, although NLFFF is a more realistic model, it also comes with many issues, such as the residual force and $\nabla \cdot \boldsymbol{B}$. If these nonphysical factors are large, they may have a significant negative impact on the simulation. The NLFFF reconstructed by `GX_Simulator` indeed contains residual Lorenz forces at the low altitudes. The current-weighted average angle between magnetic field and current density, $\langle \sin\theta \rangle$, turns out to be as high as 0.43. This is tolerated as a trade-off of the optimization between the forced photospheric magnetic field and the force-free coronal field (Fleishman et al. 2019), but may make the current simulation unstable. Since the major photospheric motions in this AR are the twisting motion on the positive polarity and the emerging motion at the PIL, which are relatively simple, we believe that the use of the potential field as the initial condition is a better choice.

The initial velocity is set to zero in the entire space, and we assume that the initial density is $\rho(\boldsymbol{x}, t=0) = |\boldsymbol{B}(\boldsymbol{x}, t=0)|$. In this case, the Alfvén speed is approximated as $|\boldsymbol{V_A}| \sim |\boldsymbol{B}|/\sqrt{\rho} = \sqrt{|\boldsymbol{B}|}$. We then add the counterclockwise rotational flow that mimics the observation shown in Figure 2(d). The rotational motion, $\boldsymbol{v}_h = (v_x, v_y)$, is given as

$$v_x = \alpha_0 \frac{\partial \Phi}{\partial y}, \quad v_y = -\alpha_0 \frac{\partial \Phi}{\partial x}, \tag{6}$$

where Φ is a stream function that satisfies $\boldsymbol{v}_h = \boldsymbol{z} \times \nabla_h \Phi$, and α_0 is a coefficient and set to 1.0×10^{-2}. It is convenient to express Φ as a function of B_z, because the twisting motion is found mainly along the contours of B_z. We thus set Φ as

$$\Phi = B_z^2 \exp\left\{\frac{-(B_z^2 - B_{z\,\max}^2)}{B_{z\,\max}^2}\right\},$$

where $B_{z\max}$ is the maximum value of B_z at the photosphere. Finally, we normalize each velocity component by the maximum value of v, i.e., $v_x \Rightarrow v_0(v_x/v_{\max})$, and $v_y \Rightarrow v_0(v_y/v_{\max})$ where $v_0 = 0.01$. We impose the rotational speed as 1% of the maximum Alfvén speed in the photosphere.

In addition to the continuous rotational flow, we introduce an emerging motion of a small bipolar flux, as obvious in the observation (Figure 2(a)). This small emerging flux has the opposite polarity (OP) compared with the preexisting flux (Kusano et al. 2012). We model its field, $\boldsymbol{B}_e$, with a torus that ascends from beneath the bottom surface of the simulation box with a velocity $\boldsymbol{v}_{\rm EM} = (0, 0, 0.01)$ (cf. Kusano et al. 2012; Muhamad et al. 2017). As a result, an electric field $-\boldsymbol{v}_{\rm EM} \times \boldsymbol{B}_e$ forms on the bottom surface.

Figure 4 shows a schematic diagram of the coordinate system used to define the small magnetic flux emergence. We first select a fixed position in the PIL ($x_{\rm PIL}$, $y_{\rm PIL}$) in the original xy Cartesian coordinate system, as the origin of the new coordinates. This position is also the center of the simulated emerging flux. For an arbitrary position (x,y) in the original coordinate system, its coordinates with respect to the new origin are $(x_d, y_d) = (x - x_{\rm PIL}, y - y_{\rm PIL})$. The new origin is kept fixed, and the azimuth angle ϕ is introduced to define the rotation of the x- and y-axes. The coordinates (x_d, y_d) then become (x_r, y_r) with respect to the new coordinate system that is obtained by rotating the x- and y-axes about the new origin counterclockwise by ϕ (Figure 4(a)), i.e.,

$$\begin{pmatrix} x_r \\ y_r \end{pmatrix} = \begin{pmatrix} \cos\phi & \sin\phi \\ -\sin\phi & \cos\phi \end{pmatrix} \begin{pmatrix} x_d \\ y_d \end{pmatrix}.$$

The simulated emerging flux region (EFR) has a hemispherical shape made of two-dimensional (2D) loops in the xz plane that are stacked along the y-axis. The magnetic field of each loop is given by $(B_{ex}, B_{ey}, B_{ez}) = B_0(-z_d/r, 0, x_d/r)$ before the rotation of the x- and y-axes. Thus, the simulated 3D EFR is

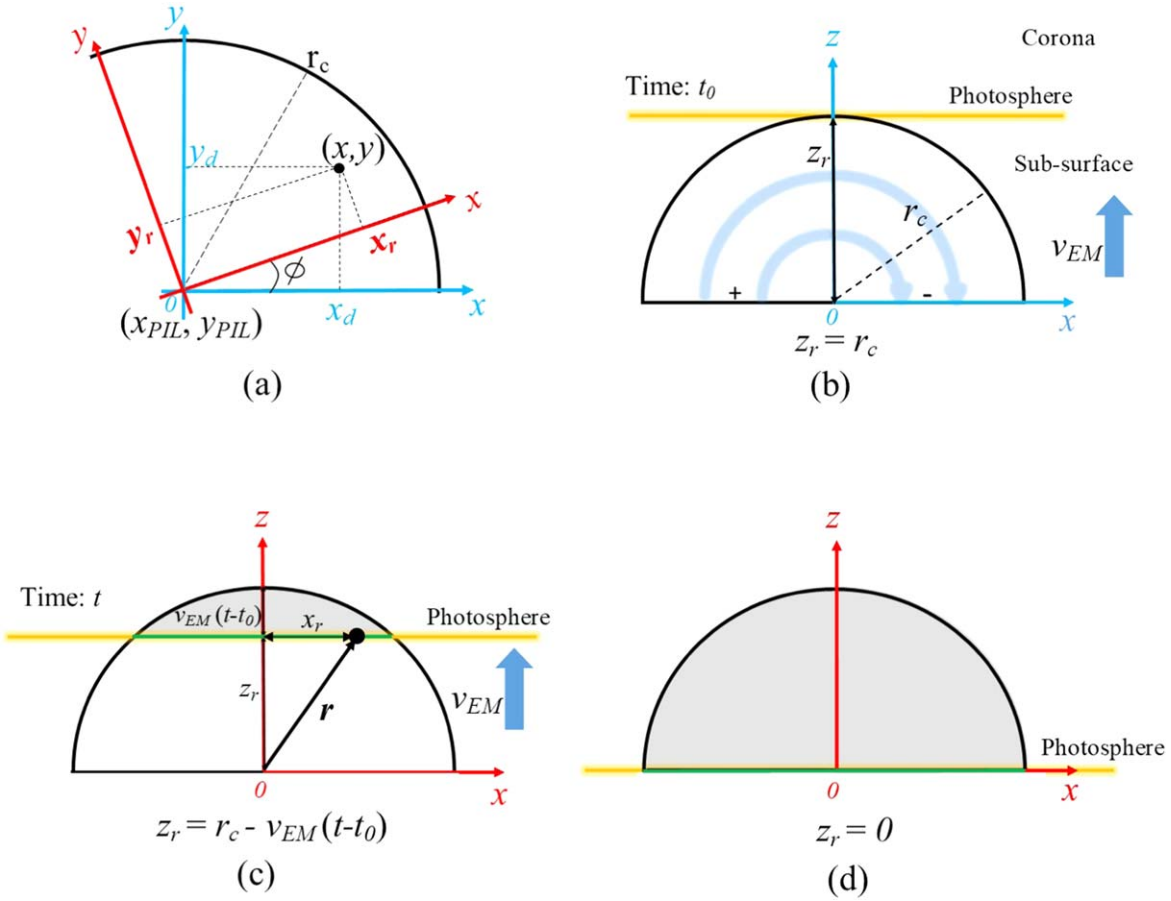

Figure 4. A schematic diagram showing the coordinates used to define the small emerging magnetic flux in the simulation. (a) A quadrant of xy Cartesian coordinate systems. A point (x, y) has coordinates (x_d, y_d) with respect to a local Cartesian coordinate system (blue) centered at $(x_{\rm PIL}, y_{\rm PIL})$. This point has coordinates (x_r, y_r) with respect to a new coordinate system (red) that is obtained by rotating the x- and y-axes through an angle ϕ. "0" denotes the origin of this new coordinate system. r_c is the maximum radius of emerging flux. (b)–(d) The simplified 2D view of the EFR (semicircle) seen in the xz plane, ascending from the subsurface to the corona, at the simulation time t_0 (when the emergence is about to start), t (emergence in progress), and at the end of the emergence, respectively. The 3D EFR is assumed to be a stack of 2D arcades along the y-direction. After the coordinate system is rotates by ϕ as shown in (a), the emergence starts. The gray shaded area shows the EFR above the photosphere. The cross section (marked by the green line) of EFR and the photosphere is given as the boundary conditions of the simulation at each time. $\boldsymbol{v}_{\rm EM}$ is the ascending velocity of EFR. At t, the height of EFR above the photosphere is $\boldsymbol{v}_{\rm EM}(t - t_0)$, while the height below the photosphere is $z_r = r_c - \boldsymbol{v}_{\rm EM}(t - t_0)$. For a position vector $\boldsymbol{r}$ at the cross section, its length is $r = \sqrt{x_r^2(t) + z_r^2(t)}$. When $z_r = r_c - \boldsymbol{v}_{\rm EM}(t - t_0) = 0$, the emergence stops, as shown in (d).

essentially a 2D structure in the xz plane extending in the y-direction. Figure 4(b) shows the simplified 2D view of the EFR (semicircle) seen in the xz plane right before the emergence. After the EFR is rotated by ϕ as shown in Figure 4(a), the magnetic field components of the EFR are expressed as

$$B_{ex}(\boldsymbol{r}, t) = -B_0 \frac{z_r(t)}{r(t)} \cos\phi,$$

$$B_{ey}(\boldsymbol{r}, t) = B_0 \frac{z_r(t)}{r(t)} \sin\phi,$$

$$B_{ez}(\boldsymbol{r}, t) = B_0 \frac{x_r(t)}{r(t)},$$

where the vector $\boldsymbol{r}$ is from the new origin to any position at the intersecting line of the 2D structure and the photosphere, with a distance of $r = \sqrt{x_r^2(t) + z_r^2(t)}$, and $z_r(t)$ measures the height of EFR below the photosphere (see Figure 4(c)). Note that, in the new coordinate system (x_r, y_r, z_r), the EFR still has the magnetic field components only in the x_r–z_r plane. We set the maximum radius of EFR to r_c, with $r_c = 0.01$. This EFR gradually ascends to the corona with a velocity of $\boldsymbol{v}_{\rm EM}$. From the time t_0 when the EFR starts to emerge to a time t, its height above and below the photosphere is $\boldsymbol{v}_{\rm EM}(t - t_0)$ and $z_r(t) = r_c - \boldsymbol{v}_{\rm EM}(t - t_0)$, respectively (Figure 4(c)). When the EFR above the photosphere reaches the height of r_c , i.e., $\boldsymbol{v}_{\rm EM}(t - t_0) = r_c$ and $z_r = 0$, the ascension of the small magnetic flux is halted (Figure 4(d)). As an example, the bipolar emerging flux at a selected time $t = 10$ in the location of $\phi = -7\pi/6$ and $B_0 = 0.5$ is shown in Figure 5(d).

All boundaries are assumed to be superconductive walls where $\boldsymbol{v}$ is zero; ρ and the normal component of the magnetic field perpendicular to each boundary are fixed while the tangential components vary according to the induction equation (Equation (3)). We impose the Neumann condition on ϕ in each boundary, i.e., $\partial\phi/\partial n = 0$ where n corresponds to normal vector perpendicular to the boundary.

Figure 5 shows the simulated evolution of magnetic field at three selected times $t = 0$, 9, and 17 in the top row (see the animation of Figure 5). In response to the sunspot rotation imposed on the boundary, the magnetic field progressively accumulates the nonpotentiality. A sigmoidal magnetic structure, made up of sheared field lines (black in Figures 5(a)–(c)

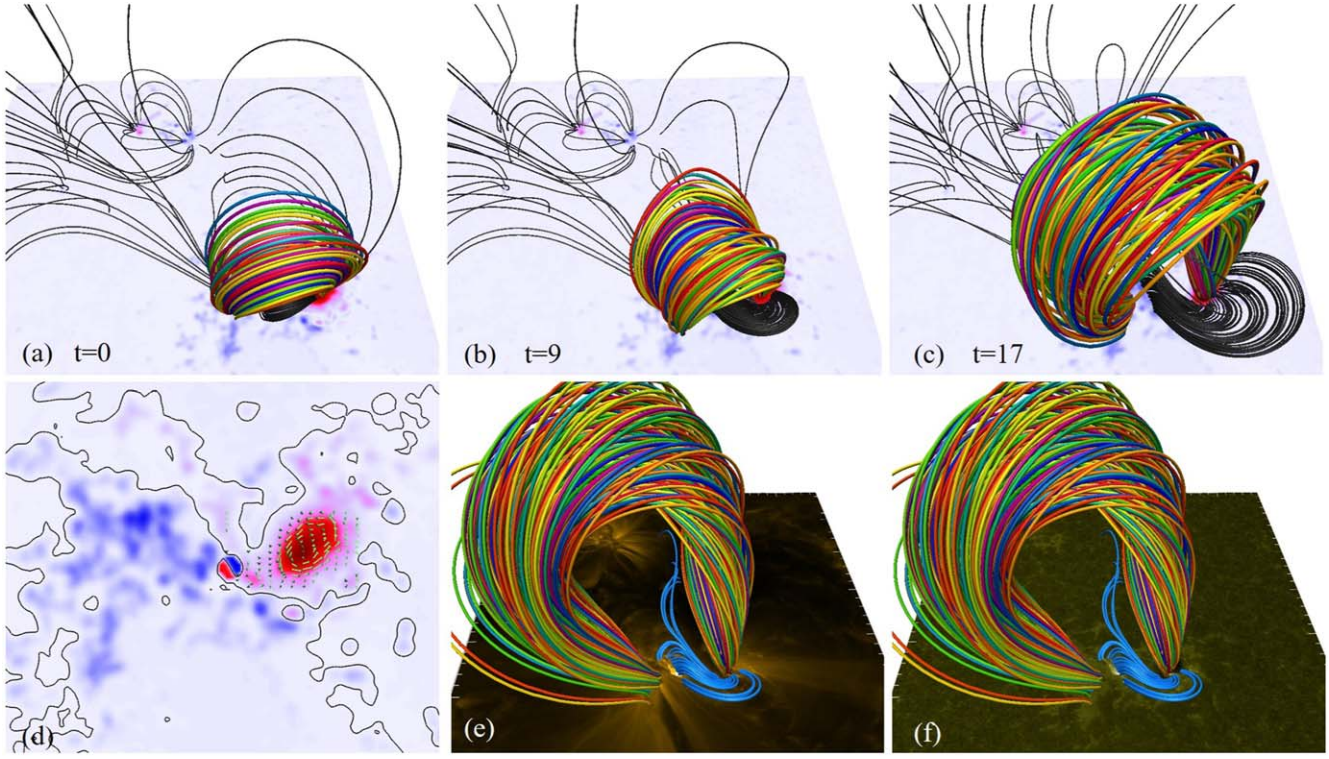

Figure 5. MHD simulation of the dynamics of magnetic field lines. (a)–(c) Snapshot of the 3D magnetic field lines with the B_z distribution at the bottom. The low-lying sigmoid field lines in the core region are depicted in black, while the CME-related erupting loops are shown in color. (d) A snapshot of the simulated sunspot rotation and flux emergence at $t = 10$. (e)–(f) 3D loops superimposed on the AIA 171 Å and 1600 Å images of 01:24 UT, 2017 July 14. The footpoints of the sigmoid field lines (blue) coincide with the flare ribbons, and the footpoints of the erupting field lines (color) coincide with that of the observed outwardly expanding coronal loop. A 1 s animation is available that shows the simulated evolution of magnetic field lines, from $t = 0$ to $t = 20$. Panels (a)–(c) are included in the animation, and panels (d)–(f) are not included in the animation.

(An animation of this figure is available.)

and blue in Figures 5(e)–(f)), is formed at the core region. The footpoints of this sigmoidal structure spatially coincide with the flare ribbons quite well (Figures 5(e)–(f)). The sigmoidal structure does not erupt, presumably because it is neither torus-unstable ($n < 1$) nor sufficiently twisted ($|T_w| < 0.5$) to trigger the kink instability. On the other hand, the overlying loop system, which is anchored at the same footpoints as the observed outwardly moving coronal loop, develops from a simply connected potential field arcade to an MFR-like structure. This MFR-like structure has an average twist number of ~ -0.75 and is situated in the torus-unstable regime with $n > 2$.

Figure 6 also shows this simulated evolution of magnetic field, with the distribution of $|\boldsymbol{J}|/|\boldsymbol{B}|$ included. During this process, the MFR is gradually moving upward. At about $t = 12$, there is a sudden increase in kinetic energy as shown in Figure 5(f), suggestive of a CME-like eruption. After $t = 13$, a vertical current sheet is formed underneath the rising MFR (Figures 6(d)–(e)). Note that the magnetic reconnection at this vertical current sheet accounts for flare ribbons and post-flare loops, but the reconnection is induced by the numerical resistive process of the eruption, rather than acting as the driver of the eruption. Thus, the flare may be a secondary effect of the CME eruption, which is also consistent with our observation that the coronal loop moves outward first, then the flare occurs.

We note that the MHD simulation reproduces the general trend of magnetic field evolution as observed, but not in every step. Specifically, the free energy predicted by the MHD simulation shows a continuous increase throughout the event (Figure 6(f)), whereas a significant release of free energy in the impulsive phase of the flare is captured by the NLFFF extrapolation (the middle panel of Figure 3(d)). This discrepancy arises from the limitation of our data-constrained simulation, i.e., the initial conditions are assumed as the potential field extrapolated from the observation, while the subsequent calculation of the magnetic field is no longer constrained by the observation. Instead, the rotational flows and emerging flux are given artificially at the photosphere. Although this data-constrained simulation cannot accommodate the abrupt change of free energy, it does predict that the growth of the free energy slows down and that of the kinetic energy is accelerated at $t = 12$ (dotted guide line in Figure 6(f)). This means that the free energy release also occurs in the simulation but is outweighed by the energy accumulation induced by the photospheric motions and flux emergence dominant in the simulation. Such an energy release implied in Figure 6(f) is certainly less obvious than that in Figure 3(d), which is a limitation of this data-constrained simulation.

To verify the cause of eruption, we performed another MHD simulations (not shown in the paper) in which we halted the driving rotational flows at $t = 13$. In this case the MFR did not erupt, but relaxed to a near potential state. This means that the eruption cannot be sustained without a constant injection of rotational flows, and that the sunspot rotation is a necessary condition for this eruption.

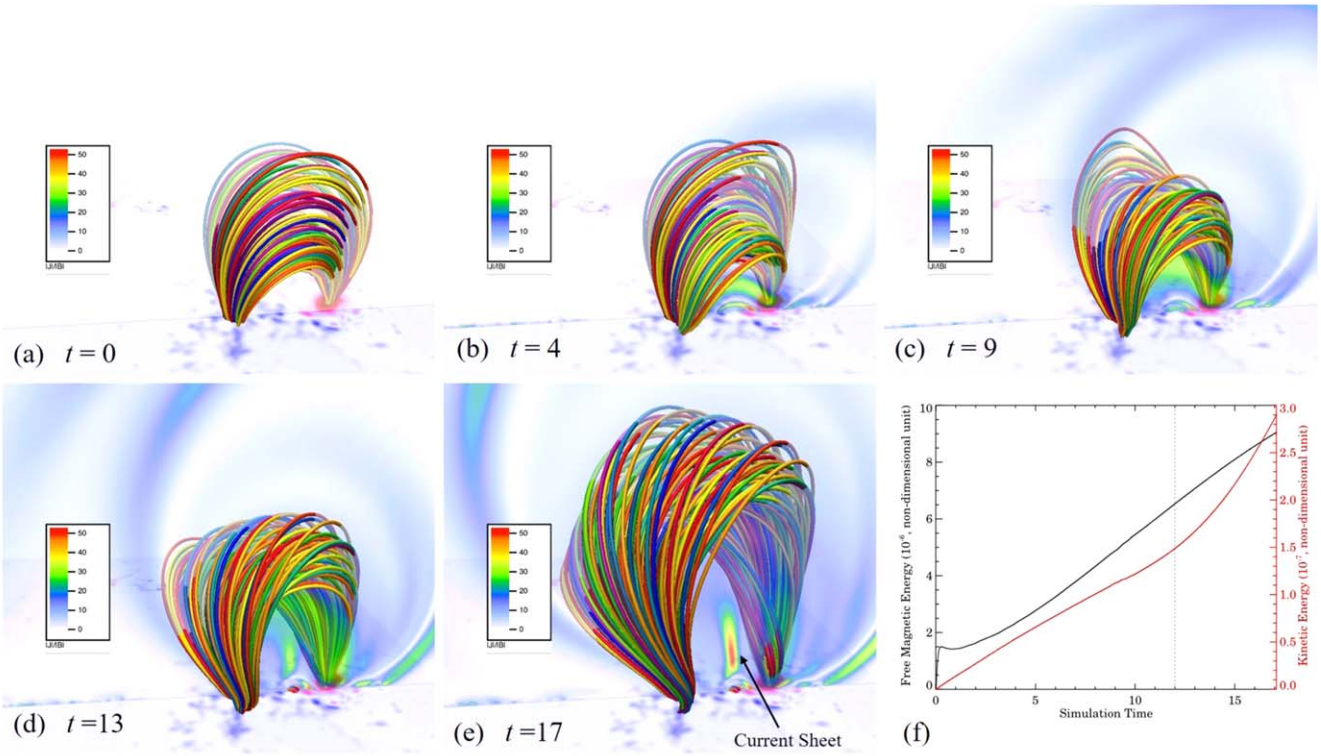

Figure 6. (a)–(e) Snapshot of the 3D magnetic field lines with the $|J|/|B|$ distribution at a vertical cross section. (f) The temporal variation of free magnetic energy and kinetic energy calculated with the simulation data. Both free magnetic energy and kinetic energy are in normalized, nondimensional units. The process is divided into two stages by the gray dotted line at about $t = 12$. A 1 s animation is available that shows the simulated evolution of magnetic field lines with the $|J|/|B|$ distribution at a vertical cross section, from $t = 0$ to $t = 20$. Panels (a)–(e) are included in the animation, and panel (f) is not included in the animation.

(An animation of this figure is available.)

4. Conclusion and Discussion

The present study aims to understand the initiation mechanism of the M2.4 flare, SOL2017-07-14T02:09, which is characterized by the magnetic eruption high in the corona along with rotation in the photosphere. For this goal, we performed an MHD simulation in which we impose the emerging magnetic flux at the PIL and a rotational flow in the sunspot similar to the observation. The simulation successfully reproduces the sigmoidal structure that accounts for the flare, and the CME-related motion of the overlying coronal loop system. The simulation shows that the overlying loop system becomes an increasingly twisted MFR as a response to sunspot rotation, then undergoes a sudden acceleration to develop a CME-like eruption. After comparing our simulation results with the observation, we conclude that essential to the initiation of this eruption is the formation of the twisted MFR above the core region due to the sunspot rotation.

In other simulations (Török et al. 2013), a sunspot rotation is introduced to weaken the magnetic tension that stabilizes the MFR. When the tension forces above the MFR are reduced to a critical point, the MHD torus instability sets in and the MFR is rapidly accelerated upward. The present simulation reproduces such a process except that the sigmoidal structure in the core region does not erupt, and the overlying MFR does. A plausible explanation is that the low-lying sigmoid remains within the torus-stable regime and does not rise to the critical height required for the onset of the torus instability ($n_{\rm crit} \geqslant 1.5$), while the high-lying MFR is torus-unstable and prone to erupt. Moreover, the sigmoidal structure is not sufficiently twisted to trigger the kink instability.

For the tether-cutting scenario, the observed OP-type emerging magnetic flux in the PIL under the sigmoidal structure is indeed suitable (Kusano et al. 2012). In the present event, however, we found no indication of tether-cutting reconnection either in the observation or in the simulation. Considering that the tether-cutting reconnection requires the small bipole of OP to connect two strongly sheared magnetic field systems (Kusano et al. 2012), it is likely that the sheared field in this case lies mainly over the small-scale and widely dispersed emerging flux and therefore cannot easily reconnect to form a long twisted MFR.

This eruptive flare is not only associated with a CME but also with a storm of SEPs. To explore the relationship between the flare and the SEP storm, we need to investigate the preexistence of a population of nonthermal seed particles accelerated during the flare. In that regard, it is worthwhile to check whether this AR had a condition favorable for the effective seeding. We plan to use this data-constrained model together with the multifrequency microwave observation with the Expanded Owens Valley Solar Array (EOVSA) to derive coronal magnetic fields and energetic particles at high-altitude parts of the eruption, so that we can determine the possible escape path for flare particles to reach the CME. Research in this direction is underway and will be presented in a separate paper.

We are indebted to the anonymous referee for the valuable comments and suggestions. We thank the NASA SDO team for HMI and AIA data. HMI and AIA are instruments on board SDO, a mission for NASA's Living with a Star program. J.J., J.

L., Q.L., C.L., Y.X., and H.W. were supported by NASA grants 80NSSC21K1671 (HSR), 80NSSC21K0003 (LWS), 80NSSC17K0016, 80NSSC18K0673, 80NSSC19K0257, 80NSSC18K1705, 80NSSC19K0859, and 80NSSC19K0068 and NSF Grants AGS 1821294, 1927578, 1954737 and NSF 2114201.

ORCID iDs

Ju Jing https://orcid.org/0000-0002-8179-3625
Satoshi Inoue https://orcid.org/0000-0001-5121-5122
Jeongwoo Lee https://orcid.org/0000-0002-5865-7924
Qin Li https://orcid.org/0000-0002-3669-1830
Gelu M. Nita https://orcid.org/0000-0003-2846-2453
Chang Liu https://orcid.org/0000-0002-6178-7471
Dale E. Gary https://orcid.org/0000-0003-2520-8396
Haimin Wang https://orcid.org/0000-0002-5233-565X

References

Amari, T., Canou, A., Aly, J.-J., Delyon, F., & Alauzet, F. 2018, Natur, 554, 211
Antiochos, S. K., DeVore, C. R., & Klimchuk, J. A. 1999, ApJ, 510, 485
Aulanier, G., Török, T., Démoulin, P., & DeLuca, E. E. 2010, ApJ, 708, 314
Bobra, M. G., Sun, X., Hoeksema, J. T., et al. 2014, SoPh, 289, 3549
Brown, D. S., Nightingale, R. W., Alexander, D., et al. 2003, SoPh, 216, 79
Carmichael, H. 1964, NASSP, 50, 451
Chen, H., Zhang, J., Cheng, X., et al. 2014, ApJL, 797, L15
Démoulin, P., & Aulanier, G. 2010, ApJ, 718, 1388
Demoulin, P., van Driel-Gesztelyi, L., Schmieder, B., et al. 1993, A&A, 271, 292
Evershed, J. 1909, MNRAS, 69, 454
Fan, Y. 2010, ApJ, 719, 728
Fan, Y., & Gibson, S. E. 2007, ApJ, 668, 1232
Fleishman, G., Mysh'yakov, I., Stupishin, A., Loukitcheva, M., & Anfinogentov, S. 2019, ApJ, 870, 101
Fleishman, G. D., Anfinogentov, S., Loukitcheva, M., Mysh'yakov, I., & Stupishin, A. 2017, ApJ, 839, 30
Hirayama, T. 1974, SoPh, 34, 323
Hiremath, K. M. 2006, JApA, 27, 277
Inoue, S., Hayashi, K., & Kusano, K. 2016, ApJ, 818, 168
Inoue, S., Hayashi, K., Magara, T., Choe, G. S., & Park, Y. D. 2014, ApJ, 788, 182
Ishiguro, N., & Kusano, K. 2017, ApJ, 843, 101
Jing, J., Liu, C., Lee, J., et al. 2018, ApJ, 864, 138
Karpen, J. T., Antiochos, S. K., & DeVore, C. R. 2012, ApJ, 760, 81
Kliem, B., Su, Y. N., van Ballegooijen, A. A., & DeLuca, E. E. 2013, ApJ, 779, 129
Kliem, B., & Török, T. 2006, PhRvL, 96, 255002
Kopp, R. A., & Pneuman, G. W. 1976, SoPh, 50, 85
Kusano, K., Bamba, Y., Yamamoto, T. T., et al. 2012, ApJ, 760, 31
Lemen, J. R., Title, A. M., Akin, D. J., et al. 2012, SoPh, 275, 17
Li, Y., Qiu, J., Longcope, D. W., Ding, M. D., & Yang, K. 2016, ApJL, 823, L13
Liu, C., Deng, N., Lee, J., et al. 2013, ApJL, 778, L36
Liu, C., Deng, N., Liu, R., et al. 2012, ApJL, 745, L4
Liu, C., Xu, Y., Cao, W., et al. 2016, NatCo, 7, 13104
Moore, R. L., Sterling, A. C., Hudson, H. S., & Lemen, J. R. 2001, ApJ, 552, 833
Muhamad, J., Kusano, K., Inoue, S., & Shiota, D. 2017, ApJ, 842, 86
Myers, C. E., Yamada, M., Ji, H., et al. 2015, Natur, 528, 526
Olmedo, O., & Zhang, J. 2010, ApJ, 718, 433
Priest, E. R., & Forbes, T. G. 2002, A&ARv, 10, 313
Schou, J., Scherrer, P. H., Bush, R. I., et al. 2012, SoPh, 275, 229
Shibata, K., & Magara, T. 2011, LRSP, 8, 6
Sturrock, P. A. 1966, Natur, 211, 695
Sun, X., Bobra, M. G., Hoeksema, J. T., et al. 2015, ApJL, 804, L28
Suryanarayana, G. S. 2010, Natur, 15, 313
Thompson, W. T. 2006, A&A, 449, 791
Török, T., & Kliem, B. 2005, ApJL, 630, L97
Török, T., Temmer, M., Valori, G., et al. 2013, SoPh, 286, 453
Wang, H., Liu, C., Ahn, K., et al. 2017, NatAs, 1, 0085
Welsch, B. T. 2018, SoPh, 293, 113
Wheatland, M. S., Sturrock, P. A., & Roumeliotis, G. 2000, ApJ, 540, 1150
Wyper, P. F., Antiochos, S. K., & DeVore, C. R. 2017, Natur, 544, 452
Yan, X. L., Qu, Z. Q., Kong, D. F., & Xu, C. L. 2012, ApJ, 754, 16
Zhang, J., & Dere, K. P. 2006, ApJ, 649, 1100
Zuccarello, F. P., Aulanier, G., & Gilchrist, S. A. 2015, ApJ, 814, 126